Layer Number Dependence of MoS_2 Photoconductivity Using Photocurrent Spectral Atomic Force Microscopic Imaging

Youngwoo Son,[†,∥] Qing Hua Wang,[†,∥,▽] Joel A. Paulson,[†] Chih-Jen Shih,[†,#] Ananth G. Rajan,[†] Kevin Tvrdy,[‡] Sojin Kim,[†] Bassam Alfeeli,[§,⊥] Richard D. Braatz,[†] and Michael S. Strano*[,†]

[†]Department of Chemical Engineering, Massachusetts Institute of Technology, Cambridge, Massachusetts 02139, United States, [‡]Department of Chemistry and Biochemistry, University of Colorado at Colorado Springs, Colorado Springs, Colorado 80918, United States, [§]KUWAIT-MIT Center for Natural Resources and Environment, Cambridge, Massachusetts 02139, United States, and [⊥]Nanotechnology and Advanced Materials Program, Energy & Building Research Center, Kuwait Institute for Scientific Research, Safat 13109, Kuwait. [∥]Y.S. and Q.H.W. contributed equally to this work. [#]Present address: Institute for Chemical and Bioengineering, ETH Zurich, HCI E 133, Vladimir-Prelog-Weg 1, CH-8093 Zurich, Switzerland. [▽]Present address: Materials Science and Engineering, School of Engineering of Matter, Transport and Energy, Arizona State University, Tempe, Arizona 85287, United States.

ABSTRACT Atomically thin MoS_2 is of great interest for electronic and optoelectronic applications because of its unique two-dimensional (2D) quantum confinement; however, the scaling of optoelectronic properties of MoS_2 and its junctions with metals as a function of layer number as well the spatial variation of these properties remain unaddressed. In this work, we use photocurrent spectral atomic force microscopy (PCS-AFM) to image the current (in the dark) and photocurrent (under illumination) generated between a biased PtIr tip and MoS_2 nanosheets with thickness ranging between $n = 1$ to 20 layers. Dark current measurements in both forward and reverse bias reveal characteristic diode behavior well-described by Fowler–Nordheim tunneling with a monolayer barrier energy of 0.61 eV and an effective barrier scaling linearly with layer number. Under illumination at 600 nm, the photocurrent response shows a marked decrease for layers up to $n = 4$ but increasing thereafter, which we describe using a model that accounts for the linear barrier increase at low n, but increased light absorption at larger n creating a minimum at $n = 4$. Comparative 2D Fourier analysis of physical height and photocurrent images shows high spatial frequency spatial variations in substrate/MoS_2 contact that exceed the frequencies imposed by the underlying substrates. These results should aid in the design and understanding of optoelectronic devices based on quantum confined atomically thin MoS_2.

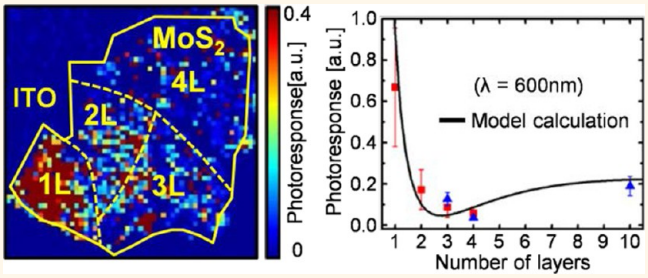

KEYWORDS: MoS_2 · layered dichalcogenide · photoconductivity · photoconductive AFM · conductive AFM · metal-MoS_2 junction

MoS_2 is a layered semiconducting transition metal dichalcogenide material whose single and few layer nanosheet forms are recently receiving significant interest as promising materials for electronic and optoelectronic devices. They have unique electronic and optical properties originating from 2D quantum confinement:[1−7] when MoS_2 is thinned to atomically thin sheets from the bulk, the optical bandgap increases and transitions from indirect to direct.[8] While MoS_2 has recently been demonstrated as the active material in a wide range of electronic[9,10] and optoelectronic[7,11−14] applications in addition to conventional field-effect transistors (FETs),[15] many questions remain about the spatial uniformity of properties across MoS_2 layers, as well as the layer number dependence of optoelectronic properties. In this work, we perform photocurrent spectral atomic force microscopy (PCS-AFM) for the first time to analyze the nanoscale junction between a conductive metal tip and MoS_2 samples varying in thickness from one (1L) to 20 layers (20L) to answer these important questions.

The layer number dependent electronic and optical properties of MoS_2 provide many interesting and important opportunities for applications in optoelectronics.

* Address correspondence to strano@mit.edu.

Received for review December 1, 2014 and accepted February 21, 2015.

Published online February 22, 2015
10.1021/nn506924j

When MoS_2 is isolated as a single layer, quantum confinement induces a transformation from an indirect bandgap of 1.3 eV for bulk MoS_2 to a direct bandgap of 1.8 eV, as has been experimentally shown, resulting in significant photoluminescence for its 1L form.[16] This behavior makes MoS_2 an intriguing candidate material in a wide variety of electronic and optoelectronic applications.[17−19] Atomically thin MoS_2 has been successfully used in digital electronic components[6,15,20−26] and circuits[10] because its sizable bandgap enables a low current in the off state, so that high on/off current ratios[15,27,28] are possible. As electronic and optoelectronic devices become smaller and smaller, the electrical contacts must also be reduced in scale. However, reducing MoS_2−metal contacts to nanometer size can produce different properties from those of the macroscopic counterparts. Moreover, the interfaces between atomically thin MoS_2 and contact and dielectric materials may differ from those with bulk MoS_2, and may have a substantial impact on the performance of devices.[29−31] Therefore, a thorough investigation of the underlying physics of the interfaces between atomically thin MoS_2 sheets of varying layer numbers and metal contacts is essential for controlling and tuning their performance.

However, there have been few studies to date that investigate charge transport behavior in the vertical direction at the nanoscale MoS_2−metal interface.[32] Thus, in this work we focus on the transverse electrical properties of nanoscale MoS_2−metal junction in the dark and under illumination of varying wavelengths using conductive and photoconductive spectral atomic force microscopy (C-AFM and PCS-AFM) measurements. By performing current imaging using a PtIr-coated conductive tip on an ultrathin MoS_2 nanosheet that contains regions of different layer thicknesses, we can form many thousands of MoS_2−metal contact points during imaging and directly compare layer-number dependent properties at the same time under the same experimental conditions with high spatial resolution. In contrast, studying these properties by the fabrication and testing of individual FET devices introduces significant complexity due to lithographic and metal deposition processes that can damage the MoS_2 sheets or change the intrinsic character of the junctions, and does not allow for spatial variations to be examined.

Li *et al.*[32] have performed a C-AFM study of multilayer MoS_2 on a Pt substrate using a CoCr conductive tip, showing that the resulting diode characteristic can be explained by the thermionic emission and the Fowler−Nordheim (FN) tunneling models for the forward and reverse tip bias regimes, respectively. However, this earlier study is not conducted on 1L and 2L MoS_2 and is limited to dark currents, leaving the influence of photoexcitation and the interesting bandgap transition unanswered. Moreover, the use of single point current−voltage (I−V) curves makes this study unable to answer questions of local spatial variations at the micro- and nanoscale.

In our work, we study for the first time the layer number dependent electrical characteristics of the MoS_2−metal nanoscale junction using current imaging of MoS_2 nanosheets consisting of regions of different thicknesses from 1L to up to 20L in both forward and reverse bias regimes using C- and PCS-AFM. By taking consecutive current images while changing bias voltages, we measure the layer number dependence of the effective barrier, showing it to be linear. We also obtain spatially resolved two-dimensional (2D) maps of local electrical properties from simultaneously recorded local I−V data. In addition, we investigate the layer number dependent spectral photoresponse of MoS_2, which showed the highest response in 1L. The photoresponse decreases for increasing layer number, but increases again between 4L and 10L due to increased light absorption. The photoresponse is also strongly dependent on the wavelength of the incident light, showing much higher currents for photon energies that are above the optical bandgap. The photoresponse in forward and reverse biases shows barrier symmetry for 1L but asymmetry for 2, 3, and 4L, which further indicates a dominant role of the barrier on carrier transport at the junction. This insight into the physical carrier transport mechanisms in MoS_2 provides critical information for further engineering MoS_2 electronic and optoelectronic devices with tuned electrical characteristics at the nanoscale level.

RESULTS AND DISCUSSION

Dark carrier transport. While the electronic properties of materials can be obtained by taking I−V curves at fixed positions of interest using C-AFM,[33−38] additional spatially resolved measurement is needed for studying spatial inhomogeneity in local charge distributions, local defects, sample edges, and local tip−sample interactions. Thus, in this work we measure the current through the C-AFM tip while imaging and varying the applied sample bias. We then average the current values across thousands of pixels or data points to obtain spatially resolved I−V characteristics of MoS_2 nanosheets.

In order to study carrier transport in the dark, MoS_2 crystals were micromechanically exfoliated onto a conductive indium tin oxide (ITO)-coated glass substrate. The crystals were first identified by optical contrast and then their layer numbers were verified using Raman spectroscopy. The C-AFM and PCS-AFM measurements were conducted using PtIr-coated conductive probes in contact mode. During the measurements, the conductive tip is held at ground while the bias voltage was applied to the ITO substrate as the other electrode. Throughout this work, we refer to forward (reverse) bias when the ITO electrode is positively (negatively) biased relative to the grounded conductive tip. More details can be found in the

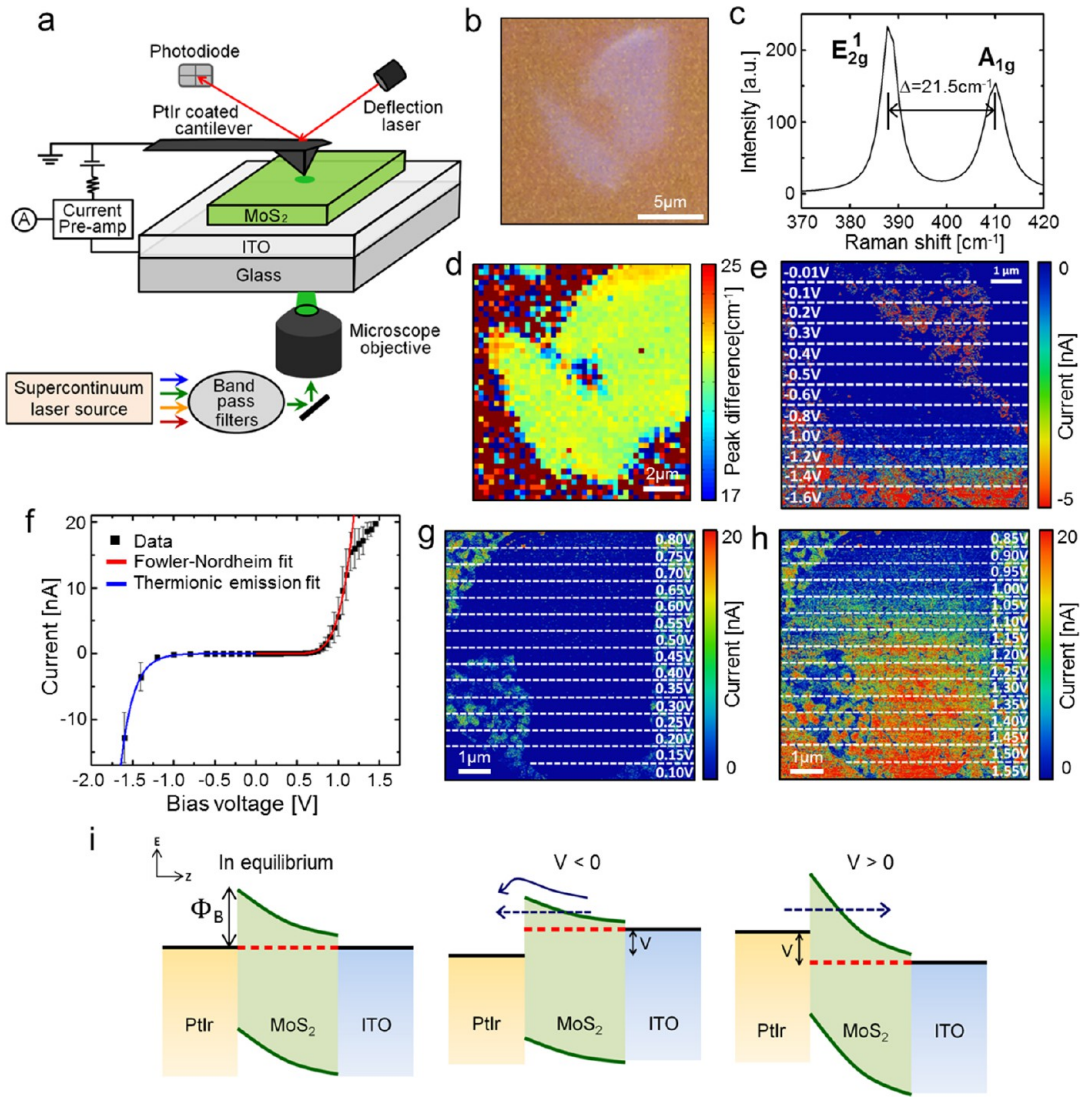

Figure 1. Conductive atomic force microscopy imaging of bilayer MoS_2. (a) A schematic of the photoconductive spectral atomic force microscope (PCS-AFM) instrument. (b) An optical microscope image of a flake of MoS_2 on ITO/glass substrate. (The contrast in the image has been enhanced to allow the flake to be more clearly seen.) (c) Raman spectrum for MoS_2 sample in (b) where the frequency difference of 21.5 cm^{-1} between E^1_{2g} and A_{1g} peaks indicates bilayer MoS_2. (d) A spatially resolved Raman map of the frequency difference shows the uniformity of MoS_2 thickness over the entire sample except for the slightly thicker region at the top edge. (e), (g)-(h) Current images in reverse bias (e) and forward sample bias (g)-(h) taken by changing the applied sample voltage within the horizontal strips. Here the bare ITO surface shows high conductivity while a noticeable nonlinear characteristic is observed in the MoS_2 flake. (f) A current−voltage (*I-V*) curve generated by taking average current values for each bias voltage from the current images where nearly insulating behavior and an abrupt nonlinear increase are observed at low and high bias voltages, respectively. The reverse bias region is fit by a thermionic emission model (blue line) while the forward bias region is fit by a Fowler−Nordheim (FN) tunneling model (red line). (i) A schematic band diagram of a thin MoS_2−metal tip junction in equilibrium (left panel) and under reverse (middle) and forward (right) sample bias voltages. The formation of a Schottky barrier impacts the carrier transport.

Methods section below. The experimental setup for our C-AFM and PCS-AFM measurements is shown in Figure 1a. The remaining panels in Figure 1 show current−voltage (*I*−*V*) characteristics for a flake of bilayer MoS_2, whose optical image is shown in Figure 1b. We identified the thickness of this flake by its Raman spectrum, where the two signature Raman peaks of MoS_2, the E^1_{2g} and A_{1g} peaks, are prominently observed, confirming that the flake is a bilayer MoS_2 crystal based on the frequency difference (Δ) of 21.5 cm^{-1},[39] as shown in Figure 1c. The spatial Raman map of Δ (Figure 1d) confirms that the entire flake is uniformly two layers thick, so that we can average spatial data across the flake and be assured that we are interrogating the same thickness of material.

In order to obtain *I*−*V* characteristics of the MoS_2-metal junction, current imaging was performed on this sample by changing the applied bias voltage in horizontal stripes, as shown in Figures 1e (reverse bias) and 1g-h (forward bias). We note that the horizontal direction is the fast scan direction, so that the voltage is being changed approximately every 30 to 40 scan lines.

In Figures 1e, g-h, the dashed lines denote the points where the bias voltage is changed and the numbers within each stripe indicates the sign and magnitude of the applied voltages. We then obtained a single $I-V$ curve by averaging the current values within each voltage stripe and within the boundaries of the MoS_2 crystal, as shown by the black data points in Figure 1f, where the error bars indicate the standard deviations from all the pixels within the current images at each given voltage. Because we have shown that the flake is uniform in thickness (Figure 1d), averaging over thousands of data points for each voltage in this way allows us to obtain a reliable $I-V$ curve.

In contrast to the bare ITO surface showing high conductivity, the MoS_2 nanosheet introduces additional resistance against current flow, exhibiting noticeable nonlinear behavior as a function of applied voltage. This response suggests the formation of an energy barrier at the nanoscale junction between the metal tip and the semiconducting MoS_2 crystal in both forward and reverse bias regimes (Figures 1e and 1g-h). The $I-V$ curve in Figure 1f shows nearly insulating behavior at low bias voltages and abrupt nonlinear increases in current at high bias voltages. Schematic illustrations in Figure 1i show the band structures of the PtIr/MoS_2/ITO system at equilibrium and under applied biases. When the metal tip is brought into contact with a thin MoS_2 crystal, the difference between its work function ($\Phi_{PtIr} = 5.4$ eV[40]) and the electron affinity of MoS_2 ($\lambda_{MoS2} = 4.5$ eV[41] for 1L to 4.0 eV[42] for bulk), based on the Schottky-Mott theory,[43] causes a Schottky barrier to form at the interface with an estimated height of about $\Phi_B = \Phi_{PtIr} - \lambda_{MoS2} = 0.9$ eV for monolayer up to 1.4 eV for bulk. The ITO substrate used in this work is a heavily n-doped with a work function of $\Phi_{ITO} \sim 4.7$ eV, resulting in a nearly ohmic contact with the atomically thin MoS_2 of $\Phi_{MoS2,\ 1L} \sim 4.7$ eV.[13,15,44] The equilibrium case of the Schottky barrier between PtIr and MoS_2 and the ohmic contact between MoS_2 and ITO is shown in the left panel of Figure 1i.

The reverse bias ($V < 0$) and forward bias ($V > 0$) band diagrams are shown in the middle and right panels of Figure 1i, respectively. In the forward bias regime, where the barrier height and direction of charge injection suppress thermionic emission to its lowest saturation, the barrier thickness is reduced with higher applied voltage (Figure 1i), resulting in an enhanced probability of field emission tunneling through the barrier. We use the Fowler–Nordheim (FN) tunneling theory, which is widely adopted as a model for describing electrons tunneling from the Fermi level of a metal to an adjacent material through a junction barrier, with the current I described by[45]

$$I(V) = \frac{A_e q^3 m V^2}{8\pi h \Phi_B d^2 m^*} \exp\left[\frac{-8\pi\sqrt{2m^*}\Phi_B{}^{3/2} d}{3hqV}\right] \quad (1)$$

where A_e denotes the effective contact area, q the electronic charge, V the applied bias voltage, h Planck's constant, Φ_B the barrier height, d the distance between the electrodes, and $m^*/m \sim 0.35$ (for 1L)[17] to 0.53 (for bulk).[32]

The experimental $I-V$ data (black squares) in Figure 1f are fit to the FN tunneling model in eq 1 (solid red line). We see that the FN model agrees well with the data, except for the deviation at higher applied biases due to the preamplifier's current limit of 20 nA. The effective barrier height formed at 2L MoS_2–metal tip junction, Φ_B, can be extracted from the fitting to the FN tunneling model to be 0.64 eV, which is lower than the value estimated by the Schottky-Mott limit. We attribute this barrier lowering to partial Fermi level pinning arising from the formation of an interfacial dipole and gap states originating from interface charge redistribution and interface hybridizations, leading to a decreased metal work function as theoretically predicted recently by Gong *et al.*[46] A small contribution may also come from defect-induced gap states due to sample imperfections. In addition, the effective junction area, A_e, is calculated to be 7.87 nm^2 from the model fit, which is close to theoretical predictions based on contact theory we performed for our system[47–49] (shown in Supporting Information), showing robustness of the measurements.

In the reverse bias regime, we use thermionic emission to model the charge transport, which was also used earlier by Li *et al.* to explain transport at the junction between a CoCr metal tip and MoS_2 samples of 3, 4, 7, and 20 layers.[32] The thermionic emission model in the reverse bias regime gives the current I and saturation current I_0 as[50]

$$I = I_0\left[\exp\left(\frac{qV}{\eta k_B T}\right) - 1\right] \quad (2)$$

where

$$I_0 = A_e A^* T^2 \exp\left(-\frac{q\Phi_B}{k_B T}\right) \quad (3)$$

and where k_B denotes the Boltzmann constant, q the electronic charge, η the ideality factor, A^* the Richardson constant (defined in the Supporting Information) and V the applied voltage.

The fit to the thermionic emission model of eq 3 is shown as the solid blue line in Figure 1f. The ideality factor η and the barrier height Φ_B can be calculated from the slope of the linear region and the saturation current I_0 as (shown in the Supporting Information):

$$\frac{1}{\eta} = \frac{k_B T}{q}\frac{d(\ln I)}{dV} \quad (4)$$

$$\Phi_B = \frac{k_B T}{q}\ln\left(\frac{A^* A T^2}{I_0}\right) \quad (5)$$

From eqs 4 and 5, we calculate the effective barrier height Φ_B to be 0.12 eV, which is significantly smaller

than that extracted in the forward voltage regime using the FN tunneling model. The ideality factor η, which is typically used to assess the deviation of current transport from the ideal thermal emission, has a value of 5.6 here, suggesting that the electron transport in the reverse regime is not fully supported simply by the conventional thermionic emission theory alone. We attribute the origin of this low Φ_B and high η to the increased probability of additional tunneling through the junction barrier, which is not considered in the conventional thermionic emission theory, as the width of the barrier for atomically thin MoS_2 is much thinner than would be expected in conventional junctions. In addition, it has been previously observed that the current behavior is increasingly dominated by tunneling as the nanoscale Schottky diode junction area becomes smaller than the depletion width.[51,52] Therefore, the conventional thermionic emission theory could underestimate Φ_B and produce a higher η than the real value, suggesting that the current transport in this bias regime has significant contributions from both tunneling through the barrier and thermionic emission.

Layer-dependent transport behavior. Since the transport of charge carriers at the nanoscale MoS_2-metal interface is determined by the barrier height and thickness, modulation of the barrier by varying the number of MoS_2 layers introduces new mechanisms for controlling the performance of electronic devices. We used a single nanosheet of MoS_2 with regions of 1, 2, 3, and 4 layers to investigate the electronic characteristics as a function of layer number. Because the same nanosheet has multiple layer thicknesses within a small area that can fit within a single AFM image, we can obtain a series of C-AFM images with varying applied biases under the same experimental conditions. Figure 2a shows an optical microscope image of the MoS_2 flake and Figure 2b is lateral force microscopy (LFM) image to more clearly show its shape. Raman spectra were taken for thickness identification (Figure 2d) where the signature peak difference (Δ) was obtained to be 18.5, 21.5, 22.5, and 23.6 cm^{-1} for 1L, 2L, 3L, and 4L, respectively. The Raman map of Δ in Figure 2c shows that the four regions are uniform in their thicknesses of 1L, 2L, 3L, and 4L.

The C-AFM images for this sample under forward bias are shown in Figures 2e–l (images for additional voltage values are presented in the Supporting Information, Figure S4). Just as was seen in Figure 1, additional resistance is introduced in the MoS_2-covered region compared to the bare ITO region. The current also increases more rapidly in the regions with thinner MoS_2 as the voltage is increased. We again produced quantitative $I-V$ curves by taking averaged currents from each region with different thicknesses for all applied bias voltages (Figure 2m), where the solid lines are fits to the FN tunneling model. The open blue triangles, purple squares and red circles indicate data points acquired from a different MoS_2 flake with 3L, 12L, and 20L regions under the same experimental conditions (additional detailed characterization for this sample can be found in the Supporting Information). Nonlinear $I-V$ behavior is obtained for all the regions, except 12L and 20L where weak or almost no current was recorded in the voltage range of our measurements. Figure 2n shows the extracted tunneling barrier term $\Phi_B^{3/2}d$, which includes contributions from both barrier height Φ_B and barrier width d by fitting to the FN tunneling model as a function of MoS_2 layer number. (The dependence of the extracted barrier heights on layer number is in the Supporting Information (S3).) The scaling is well described by

$$\Phi_B^{3/2}d = an + b \tag{6}$$

with $a = 0.26$ $eV^{3/2}$ nm and $b = 0.63$ $eV^{3/2}$ nm. As the layer number increases from 1L to 4L, $\Phi_B^{3/2}d$ increases in a linear fashion so that tunneling current is almost suppressed when MoS_2 becomes as thick as 20L.

Spatial variations in the electronic properties can be studied along with the topography of the sample because we have recorded local $I-V$ characteristics across the material. Figure 2o shows the spatially resolved map of local tunneling barrier, $\Phi_B^{3/2}d$, generated by fitting the recorded local $I-V$ information to the FN tunneling model. The general increasing trend with layer number is clearly seen in this map, showing that our model is able to capture the layer-dependent transport behavior. We note that there is some small degree of spatial inhomogeneity that may result from variations in local barrier heights arising from impurities, defects, and fluctuations in tip–sample contact.

In order to exclude the possibilities of tip degradation affecting the current measurements, a series of force–distance curves were measured directly before and after each of the 20 images appearing in Figure 2e–l and Figure S2b–g, as shown in the inset in Figure S1. No noticeable change in the interaction between the tip and the sample was observed throughout the whole experiment, with the images staying stable and sharp, suggesting that the measurements were reliable and not deteriorated by tip degradation.

Spectral photoresponse of MoS_2. The layer-dependent optoelectronic properties of atomically thin MoS_2 have attracted increasing interest, and so we also explore the spectral response of photoconductivity as a function of MoS_2 layer number. We use the same MoS_2 nanosheet that was featured in Figure 2 for these optoelectronic measurements in order to directly compare the results to the dark current behavior. Figure 3a shows a schematic illustration of the 1L, 2L, 3L, and 4L regions of this sample. Figures 3b-f and S5 are spatially resolved maps of local photoresponse under $\lambda = 550$, 600, 650, 700, 750, and 800 nm laser illumination,

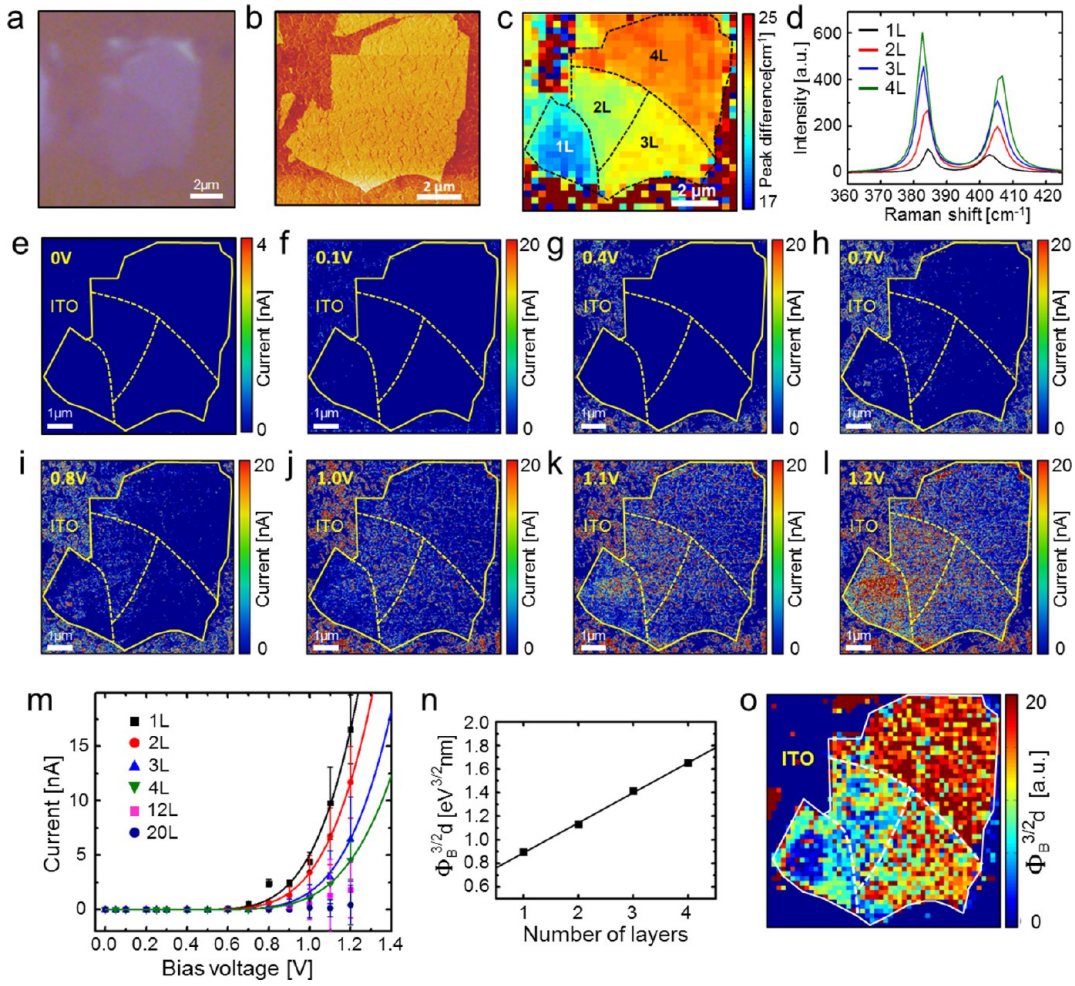

Figure 2. Layer number dependence of carrier transport in MoS_2. (a) An optical microscope image of an exfoliated sheet of MoS_2 on ITO/glass substrate consisting of 1-, 2-, 3- and 4-layer regions. (The contrast in the image has been enhanced to allow the flake to be more clearly seen.) (b) A lateral force microscopy (LFM) image for better visualization of the flake shape. We note that the LFM contrast does not allow the flake thicknesses to be clearly distinguished, but the roughness of the underlying ITO substrate is visible through the flake. (d) Representative Raman spectra taken at each region where the signature peak difference (Δ) was obtained to be 18.5, 21.5, 22.5, and 23.6 cm^{-1} indicating 1L, 2L, 3L, and 4L, respectively. (c) Raman map of Δ confirms that thickness of the nanosheet is uniform within each of the regions. (e)-(l) Current maps generated by conductive AFM measurements in the dark under applied sample bias voltages of (e) 0 V, (f) 0.1 V, (g) 0.4 V, (h) 0.7 V, (i) 0.8 V, (j) 1.0 V, (k) 1.1 V, and (l) 1.2 V. The current increases more rapidly in regions with fewer layers of MoS_2 as the applied voltage is raised. (m) Averaged $I-V$ data from regions of MoS_2 that are 1L, 2L, 3L, 4L, 12L, and 20L thick. The data for 1L to 4L are fit to the FN tunnelling model (solid lines). We note that the 12L and 20L regions are not from this particular MoS_2 nanoflake and were from another sample. (n) A plot of the tunneling barrier ($\Phi_B^{3/2}d$) extracted using the FN tunneling model as a function of MoS_2 layer number n. There is a linear dependence of effective barrier on layer number. (o) Spatially resolved map of local tunneling barrier, $\Phi_B^{3/2}d$, obtained from local $I-V$ data recorded where some degree of spatial variation is observed over the sample, but is relatively uniform within each layer thickness. The layer number dependence is again clearly seen.

where the photoresponse is defined as the difference between photocurrent (I_L) and dark current (I_D) normalized by illumination power:

$$\text{photoresponse} = \frac{(I_L - I_D)/q}{P_{inc}/h\nu} \qquad (7)$$

where q is electronic charge, P_{inc} the incident power, and $h\nu$ the photon energy. These photoresponse maps are generated by subtracting a photocurrent map under illumination from a dark current map, and normalized by the incident laser power at each wavelength. (All current images in both light and dark are shown in the Supporting Information.) A moderate bias of −0.6 V is applied throughout all the measurements to efficiently separate photoexcited charge carriers. In the photoresponse maps, a much stronger response is observed in the 1L region than in the 2L, 3L, and 4L regions as the illumination wavelength decreases from λ = 700 to 650 nm and below. In general, the photoresponse increases nonlinearly in all the regions with decreasing incident laser wavelength (increasing incident photon energy).

The spectral photoresponse as a function of incident light wavelength was plotted by taking the average

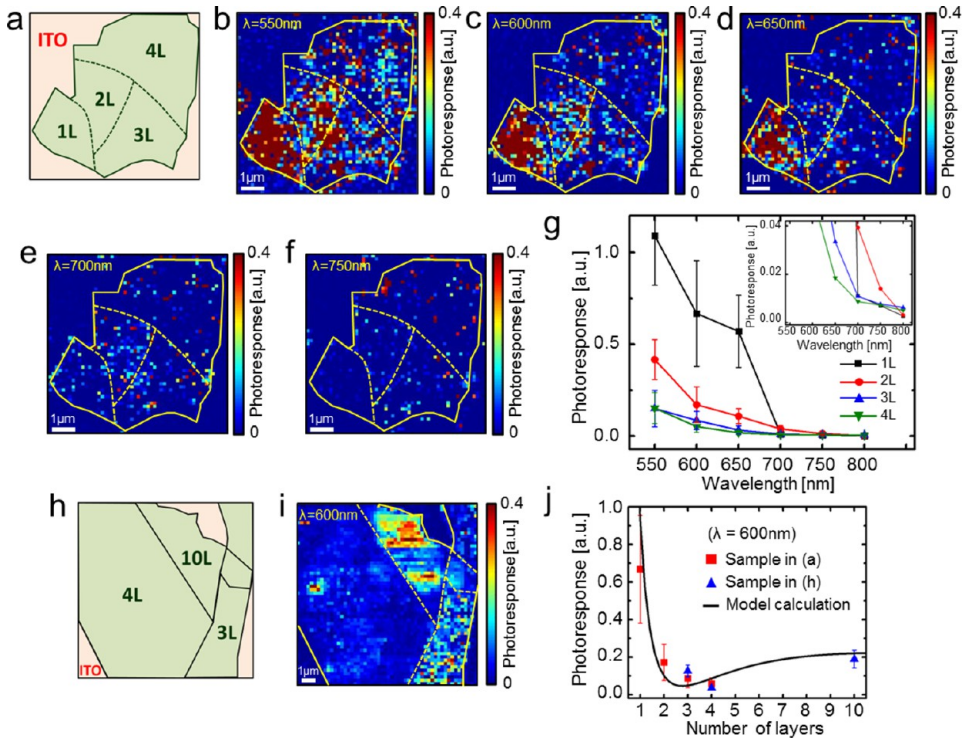

Figure 3. Spectral photoresponse in MoS_2 as a function of layer number. (a) Schematic illustration of the same MoS_2 nanosheet as shown in Figure 2, indicating the regions of different layer numbers. (b)-(f) Spatially resolved maps of local photoresponse obtained under laser illumination of (b) λ = 550 nm, (c) 600 nm, (d) 650 nm, (e) 700 nm, and (f) 750 nm. Photoresponse was obtained by subtracting dark current images from illuminated current images and normalized by the incident laser power. (g) Plot of averaged photoresponse as a function of incident laser wavelength, showing prominent layer number dependence. Error bars indicate standard deviations. The inset shows the low photoresponse range, where 3L and 4L show weak photoresponse upon illumination at λ = 800 nm while nearly no response is observed in both 1L and 2L. (h) Schematic illustration of another MoS_2 flake that consists of 3L, 4L, and 10L regions. (i) Photoresponse map of the MoS_2 flake in (h) with applied bias of -0.6 V under laser illumination of λ = 600 nm. (j) Plot of photoresponse as a function of MoS_2 layer number generated from the both samples where red and blue data points are extracted from samples in (a) and (h), respectively. The photoresponse shows evident increase in 10L after experiencing continued decrease with layer number to the lowest in 4L. We model this behavior as the effect of changing effective barrier height and optical absorption as a function of layer number (solid line).

photoresponse over each thickness region, as shown in Figure 3g, where error bars indicate the standard deviation. The inset of Figure 3g shows a magnification of the low photoresponse range. These spectral photoresponse curves demonstrate clear onsets of photoresponse at different wavelengths for each thickness, indicating the important role of the thickness-dependent band structures and tunneling barriers, which affect the photoexcitation and photocarrier collection efficiencies, respectively.

The 3L and 4L regions demonstrate weak photoresponse at λ = 800 nm ($h\nu$ = 1.55 eV) while there is nearly no photoresponse in the 1L and 2L regions because they have very low levels of light absorption and because the photon energy is below the bandgap. The 2L curve shows a prominent increase in photoresponse as the wavelength is decreased to λ = 750 nm ($h\nu$ = 1.65 eV) which agrees well with the onset of photoconductivity for 2L-MoS_2 reported in the literature occurring at about 1.6 eV,[19] whereas the response in 1L still remains at a very low level. However, as the illumination wavelength decreases further to λ = 650 nm ($h\nu$ = 1.91 eV), now coinciding with bandgap of 1L MoS_2, the photoresponse dramatically rises by a factor of about 55. At that energy above the bandgap of all the layer numbers, the 1L still has markedly the highest photoresponse because it has a direct bandgap rather than an indirect one, making the photoexcitation process much more efficient.

The decreasing trend of photoresponse with the layer number can also be explained by increasing tunneling barrier lowering the carrier collection efficiency. Despite having the weakest light absorption, monolayer MoS_2 has the highest photoresponse because its effective tunneling barrier ($\Phi_B^{3/2}d$) at the metal−MoS_2 junction is the lowest, allowing for more efficient collection of photoexcited charge carriers *via* tunneling. The decreasing trend of spectral photoresponse with illumination wavelength can also be explained using the band diagram at the junction between MoS_2 and the metal tip shown earlier in Figure 1i. In the reverse bias regime, excess energy is required for photoexcited charge carriers to overcome the barrier (solid arrow) or tunnel (dashed arrow)

through the barrier formed at the junction in order to contribute to the photocurrent. Hence an incident photon with higher energy (*i.e.*, shorter wavelength) can induce higher photoconductivity by transferring more excess energy to hot carriers, which then enhances the probability of overcoming or tunneling through the barrier. This picture of layer-dependent barrier changes is in accordance with the continued photoresponse enhancement we see in Figure 3g as the light wavelength decreases further from $\lambda = 650$ nm ($h\nu = 1.91$ eV) to 550 nm (2.25 eV), so that the photon energy is above the optical bandgap for all thicknesses.

The photoresponse appears to increase even further with the wavelength of illumination changing to $\lambda = 550$ nm from $\lambda = 600$ nm, which may be ascribed to a specific effective barrier height remaining at an applied bias of -0.6 V. In other words, Φ_B under applied bias voltage of -0.6 V is close to the amount of excess energy that incident photons of $\lambda = 550$ nm can transfer to the hot carriers such that the probability for the carriers to surmount the barrier is substantially increased at this point. It is also important to note that the wavelength dependence of photoconductivity strongly suggests the enhanced current under illumination is predominantly due to interband photoexcitation in MoS_2 rather than absorption or heating effects in the metal tip.

Additionally, an interesting increase in the photoresponse is observed as the thickness of MoS_2 increases from 4L to 10L. Figure 3h shows a schematic of another MoS_2 crystal containing regions of 3L, 4L, and 10L. Figure 3i shows the photoresponse map of this flake with applied bias of -0.6 V under laser illumination of $\lambda = 600$ nm. (Detailed optical microscopy, AFM topography and Raman analysis for layer number identification for this sample are provided in the Supporting Information.) The plot of photoresponse as a function of layer number in Figure 3j is generated from the samples in Figures 3a and 3h (red and blue data points, respectively). The photoresponse decreases sharply from 1L, but then increases again at 10 L. The photoreponse ratio, normalized to the lowest measured value for 4L, is about 15:4:2:1:4 for thicknesses 1L:2L:3L:4L:10L. Zhang *et al.*[53] and Tsai *et al.*[54] studied photoresponse of single layer and few-layer MoS_2, respectively, using similar phototransistor device architecture where the photoresponse from single layer MoS_2-based device is observed to be higher than that from few-layer MoS_2, which is dissimilar from our observation due to the different junction characteristics and experimental conditions. However, a direct and accurate comparison between two separately fabricated devices across two full publications may hardly be made, illustrating the conventional difficulty in extracting authentic layer number properties for 2D materials when one must rely on device fabrication and operation. The layer number dependence that we show for MoS_2 in our current work corresponds to the 2D material studied under identical conditions on the same substrate, varying only the layer number systematically through $n = 20$.

We ascribe this nonmonotonic photoresponse curve to the competition between carrier transport and light absorption contributions to the photocurrent. As the MoS_2 thickness increases, the tunneling barrier increases and causes the probability of excited charge carrier collection to decrease. At the same time, the amount of light absorption increases because there are more layers of material to absorb light, resulting in more carriers being photoexcited. Between 4L and 10L, enough additional hot carriers are created to lead to a rebound in the photoconductivity despite the larger tunneling barrier. We assume that light absorption is approximately proportional to layer number and that the photoexcited carriers increase the electrostatic potential of MoS_2 at the junction to provide an additional voltage. The effective bias voltage under illumination can be expressed as

$$V_{\text{eff}} = V + n\alpha \tag{8}$$

where V denotes the applied bias, n the layer number and α the additional voltage generated due to photoexcitation of carriers in a single layer of MoS_2. We also allow for the fact that the effective barrier height may be altered under photoexcitation between the single particle (dark) and two particle (illuminated) experiments.

According to the FN tunneling model, the current with and without illumination, denoted by L (light) and D (dark), are

$$I_L = \gamma_L \frac{(V+\alpha n)^2}{n^2} \exp[-\beta_L n/(V+\alpha n)] \tag{9}$$

and

$$I_D = \gamma_D \frac{V^2}{n^2} \exp[-\beta_D n/V] \tag{10}$$

respectively, where we also define the variables γ and β with and without illumination as functions of the barrier height Φ_B as

$$\gamma_{L/D} = (A_e q^3 m)/(8\pi h m^* \Phi_{B,L/D}) \tag{11}$$

$$\beta_{L/D} = (8\pi\sqrt{2m^*}\Phi_{B,L/D}^{3/2})/3hq \tag{12}$$

The photoresponse is then calculated as

$$\Delta I' = \frac{I_L - I_D}{\gamma_L V^2} = \frac{(1+\alpha' n)^2}{n^2} \exp\left[-\frac{\beta'_L n}{1+\alpha' n}\right] - \frac{\gamma'}{n^2} \exp\left[-\frac{\beta'_L n}{\gamma'^{3/2}}\right] \tag{13}$$

where we also define the terms $\gamma' = \gamma_D/\gamma_L (= \Phi_{B,L}/\Phi_{B,D})$, $\alpha' = \alpha/V$, and $\beta'_{L/D} = \beta_{L/D}/V$. The photoresponse calculated by this model is shown as the black curve in

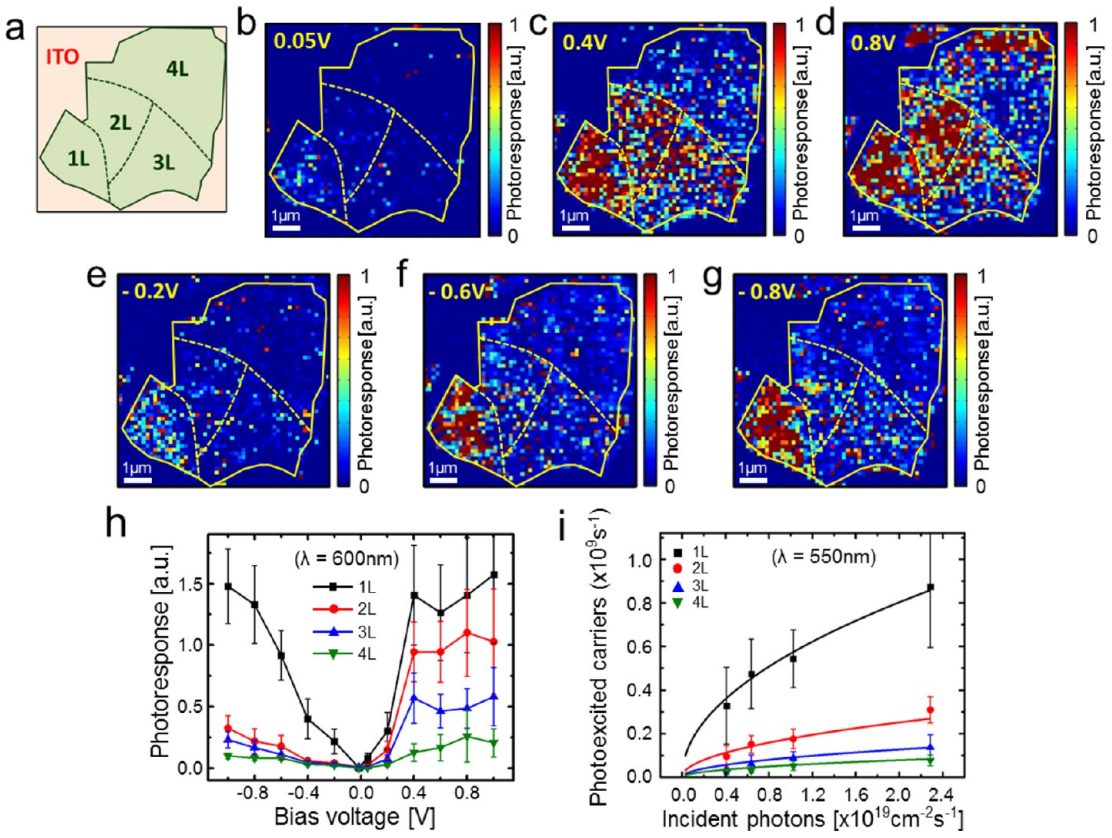

Figure 4. Dependence of photoconductivity on bias voltage and incident laser power. (a) Schematic illustration of the MoS_2 flake first shown in Figure 2, indicating layer numbers in different regions. (b)-(g) Photoresponse maps of the flake in (a) at forward bias voltages of (b) 0.05 V, (c) 0.4 V, and (d) 0.8 V, and reverse bias voltages of (e) −0.2 V, (f) −0.6 V, and (g) −0.8 V under illumination of $\lambda = 600$ nm. (h) Plot of photoresponse *versus* voltage with the error bars indicating standard deviations. We observe barrier symmetry for 1L regions but significant asymmetry is observed for 2L, 3L, and 4L regions. (i) A plot of photocurrent as a function of incident laser power density where solid lines are fit to the suggested model.

Figure 3j as a fit to the experimental data (with fitting parameters $\gamma' = 1.5$, $\beta'_L = 0.2$ and $\alpha' = 0.5$). The fit supports our model that photoresponse plummets with increasing layer number due to increased tunneling barrier up to about 3L, but rebounds as the layer number further increases because of increased light absorption. For higher values of n, the photoresponse saturates at a constant value. The results suggest an FN tunneling barrier that increases 50% upon illumination, but in a device that otherwise behaves the same in the dark state. Possible origins for this 50% increase may be photothermal, since absorption of the incident energy can result in a lattice deformation that can increase the tunneling distance (d) and increase the effective barrier.

This analysis can be expanded to interpret the strong dependence of the photocurrent on the applied voltage. Figures 4b-g show the photoresponse maps of the sample shown in Figure 3a, in both forward (b-d) and reverse voltage regimes (e-g). The bias voltages are varied while the illumination is maintained at $\lambda = 600$ nm (see the Supporting Information for additional photoresponse images at different voltages as well as current images in dark and light). The plot of photoresponse as a function of voltage is shown in Figure 4h with the error bars indicating standard deviations. We note that the photoresponse in forward and reverse bias regimes shows barrier symmetry for 1L but noticeable asymmetry is observed for 2L, 3L, and 4L.

In general, the photoresponse is stronger in forward than in reverse bias, which is likely attributed to the different barriers that form at the MoS_2−metal tip and MoS_2−ITO junction. By applying forward bias, as depicted in Figure 1i, no appreciable barrier forms at MoS_2−ITO junction, thereby enabling efficient electron collection at the ITO electrode while a large barrier forms toward the opposite direction from MoS_2 to the metal tip. The photoresponse rises sharply with voltage until around 0.4 V and becomes relatively flat, without showing notable increase afterward in all the regions. It may be because the 0.4 V bias voltage provides enough energy to separate and collect most of the photoexcited charge carriers. In reverse bias, however, separated charge carriers face a barrier at the MoS_2−metal tip junction that needs to be thermally overcome or tunneled through, and the barrier that remains in the voltage range of our experiment can lead to the observed forward−reverse asymmetry. As the applied voltage becomes more negative,

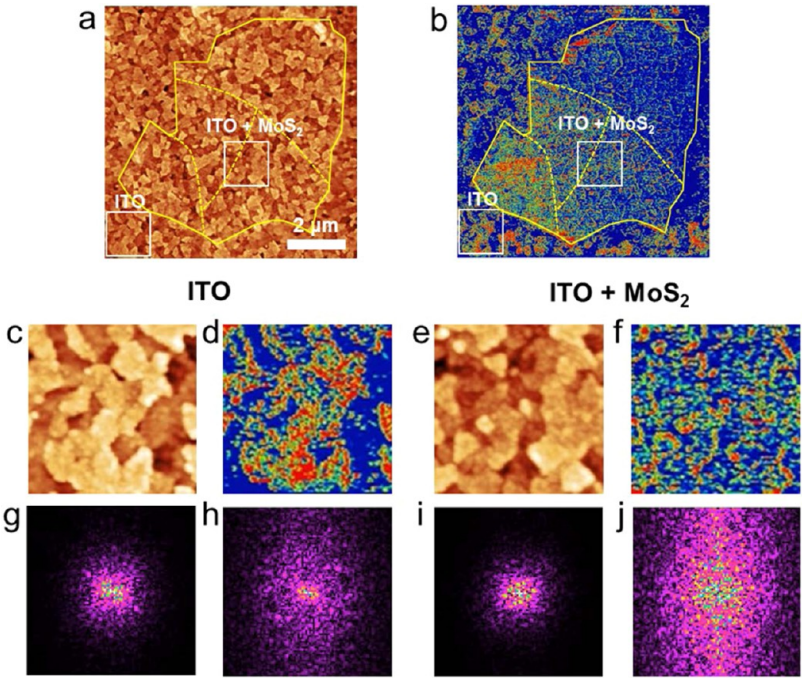

Figure 5. Spatial analysis of topography and current images. (a) Topographic height AFM image of the MoS_2 flake shown in Figure 2. (b) Current image of the same flake, at sample bias of 1.2 V. The regions in squares marked ITO and ITO+MoS_2 are regions of bare ITO and ITO covered by the MoS_2 flake, respectively. The ITO-only region is enlarged in (c)-(d) and the ITO+MoS_2 region in (e)-(f). The topographic images (c) and (e) appear quite similar. The current image (d) shows spatial correlation with the grains or terraces in (c), but the current image (f) shows less clear correlation with (e), and has more inhomogeneity in current. (g)-(j) 2D fast Fourier transforms (FFTs) of the images in (c)-(f). The FFT patterns of the topographic images (g) and (i) are quite similar, and show a relatively isotropic distribution of features. The FFT patterns of the current images (i) and (j) show differences: the FFT of ITO+MoS_2 has a lot more intensity in the vertical direction, suggesting increased inhomogeneity in the horizontal direction of the current image, corresponding to the fast scan direction. We attribute the current inhomogeneity to small amounts of crinkling in the MoS_2 flake under the tip as it scans across the surface, resulting in more variable electrical contact.

enhanced thermal emission because of the reduced barrier height competes with the lowered tunneling probability caused by the widened barrier. However, because the 1L MoS_2 is so thin, the impact of bias on the tunneling probability is minimal such that at around −0.8 V the photoresponse reaches close to the saturation level of the forward bias. In contrast, the 2L, 3L, and 4L photoresponses remain below their forward bias values due to the increased barrier thickness.

The influence of illumination power on photoresponse is shown in the photoresponse maps of Figure S10 and the plot in Figure 4i. The laser power was varied for a constant wavelength of λ = 550 nm and applied bias of −0.6 V. In general, we observe a clear increasing trend in photoconductivity for all MoS_2 thickness regions as the power increases, although some degrees of spatial irregularities exist due to local variability of electrical properties of the junction. The photocurrent shows a sublinear dependence on the incident laser intensity, where power exponents range from 0.56 to 0.67 (see the Supporting Information (S10)). We assign this nonlinear scaling of the photocurrent to the recently identified rapid exciton−exciton annihilation (EEA) in atomically thin MoS_2 crystals.[55] The exciton density can be expressed with loss terms by the EEA and exciton dissociation, and a generation term which is dependent on the laser power and the layer number:

$$\frac{dN}{dt} = -k_1N^2 - k_2N + G \tag{14}$$

$$I_{pc} = k_2N \tag{15}$$

Where k_1 is the EEA rate constant, k_2 is the free carrier generation rate (dissociation of exciton), and I_{pc} denotes photocurrent. At steady-state from 14:

$$N = -\frac{1}{2}\frac{k_2}{k_1} + \sqrt{\frac{1}{4}\left(\frac{k_2}{k_1}\right)^2 + \frac{G}{k_1}} \tag{16}$$

where $G = I_0\varepsilon(n)\Delta dn$ where I_0 denotes the incident power, $\varepsilon(n)$ (= $\varepsilon_0 n^{-4}$) the layer dependent extinction coefficient at 550 nm which demonstrates this −4 scaling for near band edge absorption, n is the number of layers, and Δd the thickness of a single layer. This model including the EEA effects generates a successful fit to the sublinear laser power-dependent photocurrent data, as represented by solid lines in the Figure 4i, where ε scales as $1/n^4$. Adopting an EEA rate constant of $k_1 = 4.3 \times 10^{-2}\text{cm}^2\text{s}^{-1}$ from Sun *et al.*,[55] k_2 and ε_0 are extracted to be $3.3(\pm0.2) \times 10^{-1}\text{s}^{-1}$ and $1.3(\pm0.2) \times 10^{-2}\text{nm}^{-1}$, respectively. The tight confidence intervals

serve to experimentally validate the exciton population balance.

Spatial analysis. We performed additional spatial analysis of the topography and current images, as shown in Figure 5, for the same MoS_2 flake that was featured in Figure 2. Two particular regions of the sample outlined in white squares are analyzed further: one indicating a region of bare ITO, and the other a region where a thin flake of MoS_2 is covering the ITO substrate. The topographic images in both regions (Figures 5c and 5e) are quite similar, with the grains or terraces of the ITO showing through the atomically thin MoS_2. The 2D fast Fourier transforms (FFTs) of these topographic images (Figures 5g and 5i) are also quite similar, with most of the intensity focused in an approximately round region in the middle, indicating anisotropic features in the original images. However, the FFT of the ITO-only current image (Figure 5h) has more intensity along the vertical direction, suggesting inhomogeneity in the horizontal direction, and the FFT of the ITO+MoS_2 current image has significantly higher intensity in the vertical direction. While there is good spatial correlation between the current and the topography for ITO alone, suggesting the currents are closely associated with the grains in the ITO, there is much less correlation in the ITO+MoS_2 case. We attribute these observations of inhomogeneity in the horizontal scan lines in Figure 5f to intermittent or imperfect contact between the MoS_2 flake and the rough ITO substrate. There is enough contact between them for the topography of the ITO to show through the atomically thin layer, but small shifts or movements between the tip, MoS_2 flake, and ITO can lead to fluctuations in the current. Because the MoS_2 sheet is so thin, we also attribute these fluctuations to crinkling of the sheet as the tip moves across in contact mode imaging.

CONCLUSIONS

In conclusion, we have studied the layer number dependent dark and photocurrent behavior at the nanometer scale junction between ultrathin MoS_2 nanosheets and metal (PtIr) using C- and PCS-AFM measurements. We measure rectifying diode characteristics, revealing that the carrier transport at the junction is successfully explained by the FN-tunneling model and thermionic emission assisted by tunneling in the forward and reverse sample bias regimes, respectively. Extracted barrier heights are about 0.3 eV lower than those predicted by the traditional metal−semiconductor contact model possibly due to partial Fermi level pinning by the formation of an interfacial dipole and gap states, and an effective tunneling barrier scales linearly with MoS_2 layer number. An outstanding photoresponse was observed in 1L MoS_2 due to its ultrathin energy barrier at the junction with the metal. Interestingly, the photoresponse as a function of increasing layer number displays the competing effects of photoexcitation efficiency dropping as the bandgap decreases and changes to indirect, and the light absorption increasing. The photoresponse symmetry in 1L and asymmetry in 2, 3, and 4L as a function of bias polarity further corroborates the picture of subtle contributions from both the thermal emission and field-effect tunneling to photocurrent transport. The sublinear power dependence of photocurrent is observed, suggesting the possible presence of trap states at the MoS_2−metal junction. Based on the fundamental understanding of the layer number dependence of electronic and optoelectronic behavior at the nanoscale MoS_2−metal junction that we have achieved in this work, the selection of the metal and controlling the MoS_2 layer number will enable a wide range of electrical property modulation that will be beneficial for future device applications.

METHODS

MoS_2 single crystal (SPI Supplies) nanosheets were deposited onto ITO-coated glass substrates (Sigma-Aldrich) by micromechanical exfoliation,[44] followed by annealing in argon at atmospheric pressure at 250 °C for 1 h in order to remove tape residues and improve the contact quality between the sample and the substrate surface. Prior to micromechanical exfoliation, the ITO/glass substrates were cleaned by sonication in acetone, then isopropanol, and blown dry by ultrapure nitrogen before cleaning in an oxygen plasma chamber (Glow Research). Atomically thin MoS_2 nanosheets were first identified by optical microscopy, followed by Raman spectroscopy to identify the number of layers by the difference (Δ) between the two signature Raman peaks of MoS_2: the in-plane vibrational E^1_{2g} and the out-of-plane vibrational A_{1g} peaks, as reported by C. Lee *et al.*[39] Raman spectroscopy was performed on a Horiba Jobin Yvon LabRAM HR800 system with 532 nm laser excitation whose output power was reduced using neutral density filters to prevent damaging the MoS_2 samples.

The C-AFM and PCS-AFM measurements were conducted on an Asylum MFP-3D system in ambient conditions, as illustrated in Figure 1a. Conductive imaging used the ORCA conductive module from Asylum and PtIr-coated probes from Bruker. Current and topographic images were obtained simultaneously so that topography and local currents can be directly compared. Most images were 512 × 512 pixels. For PCS-AFM, the instrument is mounted on an inverted optical microscope (Zeiss) with a 50X objective to focus light through the glass substrate at the tip−sample junction. The illumination source was a supercontinuum laser (SuperK Extreme from NKT Photonics), filtered by bandpass filters (fwhm = 10 nm; Thorlabs, Inc.) to illuminate the sample at selected wavelengths. During certain measurements, neutral density filters were used to modulate the laser intensity. AFM images were analyzed and plotted using the Gwyddion software package,[56] which was also used to calculate the 2D fast Fourier transforms and root-mean-square roughness values.

Conflict of Interest: The authors declare no competing financial interest.

Acknowledgment. M.S. Strano acknowledges a grant from Eni S.p.A. through the MIT Energy Initiative Program and the GATE-MURI program funded by the Office of Naval Research. This work was supported in part by the U.S. Army Research Laboratory and the U.S. Army Research Office through the Institute for US Soldier Nanotechnologies, under contract number W911NF-13-D-0001. Y. Son is grateful for partial financial support from the Samsung Scholarship.

Supporting Information Available: Estimation of effective contact area, calculation of ideality factor and barrier height, additional sample characterization and conductive and photocurrent spectral AFM images. This material is available free of charge *via* the Internet at http://pubs.acs.org.

REFERENCES AND NOTES

1. Mattheiss, L. F. Energy Bands for 2*H*-$NbSe_2$ and 2*H*-MoS_2. *Phys. Rev. Lett.* **1973**, *30*, 784–787.
2. Mak, K. F.; He, K.; Shan, J.; Heinz, T. F. Control of Valley Polarization in Monolayer MoS_2 by Optical Helicity. *Nat. Nanotechnol.* **2012**, *7*, 494–498.
3. Zeng, H.; Dai, J.; Yao, W.; Xiao, D.; Cui, X. Valley Polarization in MoS_2 Monolayers by Optical Pumping. *Nat. Nanotechnol.* **2012**, *7*, 490–493.
4. Mak, K. F.; He, K.; Lee, C.; Lee, G. H.; Hone, J.; Heinz, T. F.; Shan, J. Tightly Bound Trions in Monolayer MoS_2. *Nat. Mater.* **2013**, *12*, 207–211.
5. Wu, S.; Ross, J. S.; Liu, G.-B.; Aivazian, G.; Jones, A.; Fei, Z.; Zhu, W.; Xiao, D.; Yao, W.; Cobden, D.; *et al.* Electrical Tuning of Valley Magnetic Moment through Symmetry Control in Bilayer MoS_2. *Nat. Phys.* **2013**, *9*, 149–153.
6. Kim, S.; Konar, A.; Hwang, W.-S.; Lee, J. H.; Lee, J.; Yang, J.; Jung, C.; Kim, H.; Yoo, J.-B.; Choi, J.-Y.; *et al.* High-Mobility and Low-Power Thin-Film Transistors Based on Multilayer MoS_2 Crystals. *Nat. Commun.* **2012**, *3*, 1011.
7. Choi, W.; Cho, M. Y.; Konar, A.; Lee, J. H.; Cha, G.-B.; Hong, S. C.; Kim, S.; Kim, J.; Jena, D.; Joo, J.; *et al.* High-Detectivity Multilayer MoS_2 Phototransistors with Spectral Response from Ultraviolet to Infrared. *Adv. Mater.* **2012**, *24*, 5832–5836.
8. Wang, Q. H.; Kalantar-Zadeh, K.; Kis, A.; Coleman, J. N.; Strano, M. S. Electronics and Optoelectronics of Two-Dimensional Transition Metal Dichalcogenides. *Nat. Nanotechnol.* **2012**, *7*, 699–712.
9. Radisavljevic, B.; Whitwick, M. B.; Kis, A. Integrated Circuits and Logic Operations Based on Single-Layer MoS_2. *ACS Nano* **2011**, *5*, 9934–9938.
10. Wang, H.; Yu, L.; Lee, Y.-H.; Shi, Y.; Hsu, A.; Chin, M. L.; Li, L.-J.; Dubey, M.; Kong, J.; Palacios, T. Integrated Circuits Based on Bilayer MoS_2 Transistors. *Nano Lett.* **2012**, *12*, 4674–4680.
11. Lee, H. S.; Min, S.-W.; Chang, Y.-G.; Park, M. K.; Nam, T.; Kim, H.; Kim, J. H.; Ryu, S.; Im, S. MoS_2 Nanosheet Phototransistors with Thickness-Modulated Optical Energy Gap. *Nano Lett.* **2012**, *12*, 3695–3700.
12. Lopez-Sanchez, O.; Lembke, D.; Kayci, M.; Radenovic, A.; Kis, A. Ultrasensitive Photodetectors Based on Monolayer MoS_2. *Nat. Nanotechnol.* **2013**, *8*, 497–501.
13. Yin, Z.; Li, H.; Li, H.; Jiang, L.; Shi, Y.; Sun, Y.; Lu, G.; Zhang, Q.; Chen, X.; Zhang, H. Single-Layer MoS_2 Phototransistors. *ACS Nano* **2011**, *6*, 74–80.
14. Sundaram, R. S.; Engel, M.; Lombardo, A.; Krupke, R.; Ferrari, A. C.; Avouris, P.; Steiner, M. Electroluminescence in Single Layer MoS_2. *Nano Lett.* **2013**, *13*, 1416–1421.
15. Radisavljevic, B.; Radenovic, A.; Brivio, J.; Giacometti, V.; Kis, A. Single-Layer MoS_2 Transistors. *Nat. Nanotechnol.* **2011**, *6*, 147–150.
16. Splendiani, A.; Sun, L.; Zhang, Y.; Li, T.; Kim, J.; Chim, C.-Y.; Galli, G.; Wang, F. Emerging Photoluminescence in Monolayer MoS_2. *Nano Lett.* **2010**, *10*, 1271–1275.
17. Cheiwchanchamnangij, T.; Lambrecht, W. R. L. Quasiparticle Band Structure Calculation of Monolayer, Bilayer, and Bulk MoS_2. *Phys. Rev. B* **2012**, *85*, 205302.
18. Kuc, A.; Zibouche, N.; Heine, T. Influence of Quantum Confinement on the Electronic Structure of the Transition Metal Sulfide TS_2. *Phys. Rev. B* **2011**, *83*, 245213.
19. Mak, K. F.; Lee, C.; Hone, J.; Shan, J.; Heinz, T. F. Atomically Thin MoS_2: A New Direct-Gap Semiconductor. *Phys. Rev. Lett.* **2010**, *105*, 136805.
20. Ayari, A.; Cobas, E.; Ogundadegbe, O.; Fuhrer, M. S. Realization and Electrical Characterization of Ultrathin Crystals of Layered Transition-Metal Dichalcogenides. *J. Appl. Phys.* **2007**, *101*, 014507.
21. Yoon, Y.; Ganapathi, K.; Salahuddin, S. How Good Can Monolayer MoS_2 Transistors Be? *Nano Lett.* **2011**, *11*, 3768–3773.
22. Li, H.; Yin, Z. Y.; He, Q. Y.; Li, H.; Huang, X.; Lu, G.; Fam, D. W. H.; Tok, A. I. Y.; Zhang, Q.; Zhang, H. Fabrication of Single- and Multilayer MoS_2 Film-Based Field-Effect Transistors for Sensing NO at Room Temperature. *Small* **2012**, *8*, 63–67.
23. Lee, K.; Kim, H. Y.; Lotya, M.; Coleman, J. N.; Kim, G. T.; Duesberg, G. S. Electrical Characteristics of Molybdenum Disulfide Flakes Produced by Liquid Exfoliation. *Adv. Mater.* **2011**, *23*, 4178–4181.
24. Das, S.; Chen, H.-Y.; Penumatcha, A. V.; Appenzeller, J. High Performance Multilayer MoS_2 Transistors with Scandium Contacts. *Nano Lett.* **2012**, *13*, 100–105.
25. Liu, H.; Ye, P. D. MoS_2 Dual-Gate MOSFET with Atomic-Layer-Deposited Al_2O_3 as Top-Gate Dielectric. *IEEE Electron Device Lett.* **2012**, *33*, 546–548.
26. Qiu, H.; Pan, L.; Yao, Z.; Li, J.; Shi, Y.; Wang, X. Electrical Characterization of Back-Gated Bi-Layer MoS_2 Field-Effect Transistors and the Effect of Ambient on Their Performances. *Appl. Phys. Lett.* **2012**, *100*, 123104.
27. Liu, H.; Neal, A. T.; Ye, P. D. Channel Length Scaling of MoS_2 MOSFETs. *ACS Nano* **2012**, *6*, 8563–8569.
28. Jariwala, D.; Sangwan, V. K.; Late, D. J.; Johns, J. E.; Dravid, V. P.; Marks, T. J.; Lauhon, L. J.; Hersam, M. C. Band-Like Transport in High Mobility Unencapsulated Single-Layer MoS_2 Transistors. *Appl. Phys. Lett.* **2013**, *102*, 173107.
29. Shih, C.-J.; Wang, Q. H.; Son, Y.; Jin, Z.; Blankschtein, D.; Strano, M. S. Tuning on−Off Current Ratio and Field-Effect Mobility in a MoS_2−Graphene Heterostructure *via* Schottky Barrier Modulation. *ACS Nano* **2014**, *8*, 5790–5798.
30. Late, D. J.; Liu, B.; Matte, H. S. S. R.; Dravid, V. P.; Rao, C. N. R. Hysteresis in Single-Layer MoS_2 Field Effect Transistors. *ACS Nano* **2012**, *6*, 5635–5641.
31. Walia, S.; Balendhran, S.; Wang, Y.; Ab Kadir, R.; Sabirin Zoolfakar, A.; Atkin, P.; Zhen, O. J.; Sriram, S.; Kalantar-zadeh, K.; Bhaskaran, M. Characterization of Metal Contacts for Two-Dimensional MoS_2 Nanoflakes. *Appl. Phys. Lett.* **2013**, *103*, 232105.
32. Li, Y.; Xu, C.-Y.; Zhen, L. Surface Potential and Interlayer Screening Effects of Few-Layer MoS_2 Nanoflakes. *Appl. Phys. Lett.* **2013**, *102*, 143110.
33. Deb, P.; Kim, H.; Qin, Y.; Lahiji, R.; Oliver, M.; Reifenberger, R.; Sands, T. GaN Nanorod Schottky and P−N Junction Diodes. *Nano Lett.* **2006**, *6*, 2893–2898.
34. Xu, D.; Watt, G. D.; Harb, J. N.; Davis, R. C. Electrical Conductivity of Ferritin Proteins by Conductive AFM. *Nano Lett.* **2005**, *5*, 571–577.
35. Andolfi, L.; Cannistraro, S. Conductive Atomic Force Microscopy Study of Plastocyanin Molecules Adsorbed on Gold Electrode. *Surf. Sci.* **2005**, *598*, 68–77.
36. Baldacchini, C.; Cannistraro, S. Conductive Atomic Force Microscopy Investigation of Transverse Current across Metallic and Semiconducting Single-Walled Carbon Nanotubes. *Appl. Phys. Lett.* **2007**, *91*, 122103.
37. Kivioja, J. M.; Kurppa, K.; Kainlauri, M.; Linder, M. B.; Ahopelto, J. Electrical Transport through Ordered Self-Assembled Protein Monolayer Measured by Constant Force Conductive Atomic Force Microscopy. *Appl. Phys. Lett.* **2009**, *94*, 183901.
38. Moore, J. C.; Kenny, S. M.; Baird, C. S.; Morkoç, H.; Baski, A. A. Electronic Behavior of the Zn- and O-Polar ZnO Surfaces Studied Using Conductive Atomic Force Microscopy. *J. Appl. Phys.* **2009**, *105*, 116102.
39. Lee, C.; Yan, H.; Brus, L. E.; Heinz, T. F.; Hone, J.; Ryu, S. Anomalous Lattice Vibrations of Single- and Few-Layer MoS_2. *ACS Nano* **2010**, *4*, 2695–2700.

40. Klaua, M.; Ullmann, D.; Barthel, J.; Wulfhekel, W.; Kirschner, J.; Urban, R.; Monchesky, T. L.; Enders, A.; Cochran, J. F.; Heinrich, B. Growth, Structure, Electronic, and Magnetic Properties of MgO/Fe(001) Bilayers and Fe/MgO/Fe(001) Trilayers. *Phys. Rev. B* **2001**, *64*, 134411.
41. Abrams, B. L.; Wilcoxon, J. P. Nanosize Semiconductors for Photooxidation. *Crit. Rev. Solid State Mater. Sci.* **2005**, *30*, 153–182.
42. Han, S. W.; Kwon, H.; Kim, S. K.; Ryu, S.; Yun, W. S.; Kim, D. H.; Hwang, J. H.; Kang, J. S.; Baik, J.; Shin, H. J.; *et al.* Band-Gap Transition Induced by Interlayer van der Waals Interaction in MoS_2. *Phys. Rev. B* **2011**, *84*, 045409.
43. Rhoderick, E. H. Metal-Semiconductor Contacts. *IEE Proc., Part I: Solid-State Electron Devices* **1982**, *129*, 1.
44. Novoselov, K. S.; Jiang, D.; Schedin, F.; Booth, T. J.; Khotkevich, V. V.; Morozov, S. V.; Geim, A. K. Two-Dimensional Atomic Crystals. *Proc. Natl. Acad. Sci. U.S.A.* **2005**, *102*, 10451–10453.
45. Fowler, R. H.; Nordheim, L. Electron Emission in Intense Electric Fields. *Proc. R. Soc. London A* **1928**, *119*, 173–181.
46. Gong, C.; Colombo, L.; Wallace, R. M.; Cho, K. The Unusual Mechanism of Partial Fermi Level Pinning at Metal−MoS_2 Interfaces. *Nano Lett.* **2014**, *14*, 1714–1720.
47. Cappella, B.; Dietler, G. Force-Distance Curves by Atomic Force Microscopy. *Surf. Sci. Rep.* **1999**, *34*, 1–104.
48. Ruskell, T. G.; Workman, R. K.; Chen, D.; Sarid, D.; Dahl, S.; Gilbert, S. High Resolution Fowler−Nordheim Field Emission Maps of Thin Silicon Oxide Layers. *Appl. Phys. Lett.* **1996**, *68*, 93.
49. Frammelsberger, W.; Benstetter, G.; Kiely, J.; Stamp, R. C-AFM-Based Thickness Determination of Thin and Ultra-Thin SiO_2 Films by Use of Different Conductive-Coated Probe Tips. *Appl. Surf. Sci.* **2007**, *253*, 3615–3626.
50. Sze, S. M.; Ng, K. K. *Physics of Semiconductor Devices*, 3rd ed.; Wiley-Interscience: Hoboken, NJ, 2007.
51. Smit, G. D. J.; Rogge, S.; Klapwijk, T. M. Scaling of Nano-Schottky-Diodes. *Appl. Phys. Lett.* **2002**, *81*, 3852.
52. Smit, G. D. J.; Rogge, S.; Klapwijk, T. M. Enhanced Tunneling across Nanometer-Scale Metal−Semiconductor Interfaces. *Appl. Phys. Lett.* **2002**, *80*, 2568.
53. Zhang, W.; Huang, J.-K.; Chen, C.-H.; Chang, Y.-H.; Cheng, Y.-J.; Li, L.-J. High-Gain Phototransistors Based on a CVD MoS_2 Monolayer. *Adv. Mater.* **2013**, *25*, 3456–3461.
54. Tsai, D.-S.; Liu, K.-K.; Lien, D.-H.; Tsai, M.-L.; Kang, C.-F.; Lin, C.-A.; Li, L.-J.; He, J.-H. Few-Layer MoS_2 with High Broadband Photogain and Fast Optical Switching for Use in Harsh Environments. *ACS Nano* **2013**, *7*, 3905–3911.
55. Sun, D.; Rao, Y.; Reider, G. A.; Chen, G.; You, Y.; Brézin, L.; Harutyunyan, A. R.; Heinz, T. F. Observation of Rapid Exciton−Exciton Annihilation in Monolayer Molybdenum Disulfide. *Nano Lett.* **2014**, *14*, 5625–5629.
56. Nečas, D.; Klapetek, P. Gwyddion: An Open-Source Software for SPM Data Analysis. *Centr. Eur. J. Phys.* **2012**, *10*, 181–188.